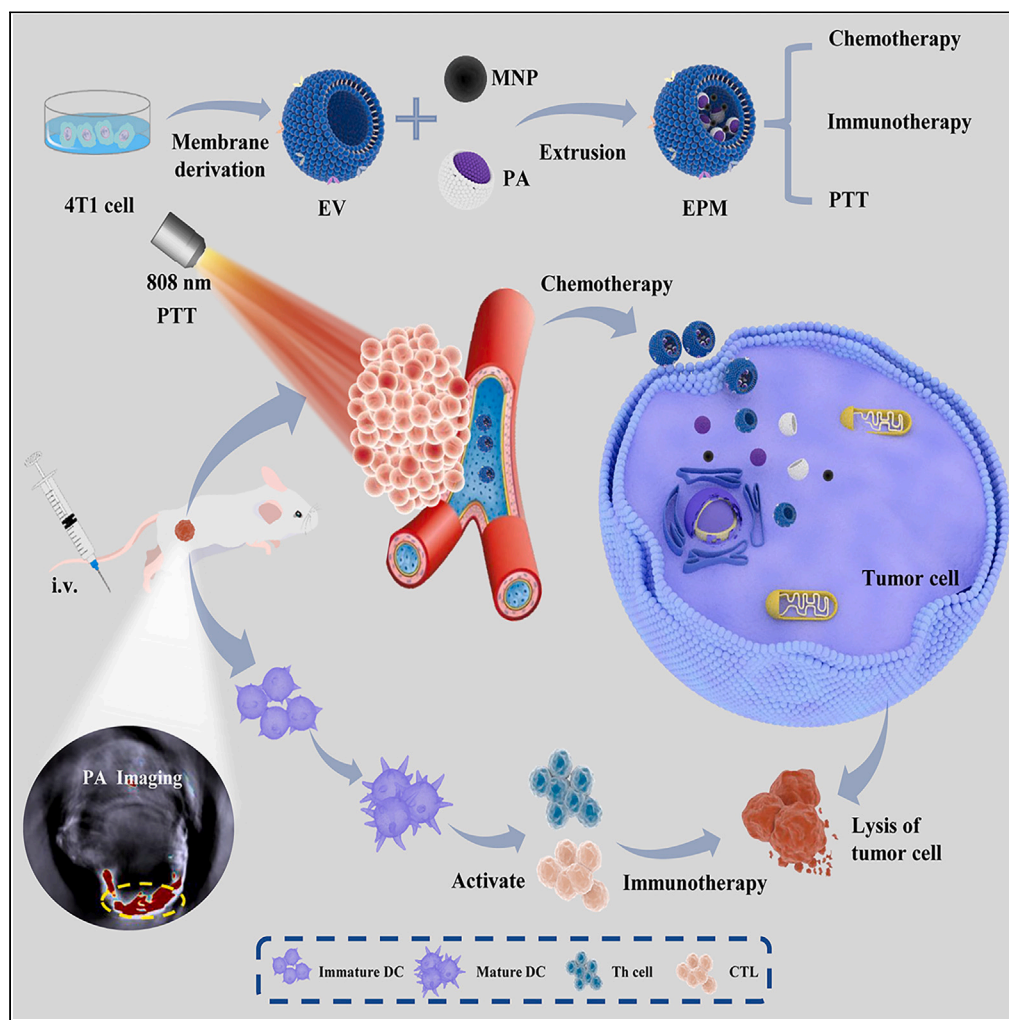


## Article

## Tumor-derived extracellular vesicle drug delivery system for chemo-photothermal-immune combination cancer treatment



Yanghui Bi, Jieya Chen, Qing Li, ..., Liu Zhida, Fajia Yuan, Ruiping Zhang

zrp\_7142@sxmu.edu.cn

## Highlights

It was developed a unique nano-drug delivery method for vesicle-loaded melanin and PA

EVs were co-extrusion with melanin and PA to produce EPM

EPM initiates a combination of chemo-photothermal-immune therapy for breast cancer

## Article

## Tumor-derived extracellular vesicle drug delivery system for chemo-photothermal-immune combination cancer treatment

Yanghui Bi,<sup>1,8</sup> Jieya Chen,<sup>2,8</sup> Qing Li,<sup>1</sup> Yan Li,<sup>3</sup> Ling Zhang,<sup>4</sup> Liu Zhida,<sup>5</sup> Fajia Yuan,<sup>6</sup> and Ruiping Zhang<sup>7,9,\*</sup>

## SUMMARY

**Tumor extracellular vesicles (EVs) demonstrate considerable promise for medication delivery and tumor targeting owing to their natural long-term blood circulation and tissue targeting capabilities. We extracted EVs from mouse breast cancer cell 4T1 using UV stimulation and differential centrifugation. To create a new nano-drug delivery system, the vesicle delivery system (EPM) loaded with melanin and paclitaxel albumin (PA), the collected EVs were repeatedly compressed on a 200 nm porous polycarbonate membrane with melanin and PA. Our findings suggest that EPM is readily absorbed by breast cancer and dendritic cells. EPM generates significant photoacoustic signals and photothermal effects when exposed to near-infrared light and can enhance the infiltration of CD8<sup>+</sup> T cells in mouse tumor tissues. EPM is more cytotoxic than PA in *in vivo* and *in vitro* investigations. The efficacy of EPM in clinical transformation when paired with chemotherapy/photothermal/immunotherapy treatment is demonstrated in this study.**

## INTRODUCTION

Breast cancer is the fifth leading cause of cancer-related deaths worldwide and poses a threat to human health.<sup>1</sup> Although clinical breast cancer treatments have progressed, recurrence, and metastasis caused by tumor heterogeneity remain challenging.<sup>2</sup> Over recent decades, nano-medicine tumor treatment strategies have received extensive attention for improving the clinical state of breast cancer. Doxil, Abraxane, DaunoXome, and other nanomedicines with varying physical properties and biological effects have been used in clinical trials.<sup>3,4</sup> Paclitaxel albumin (PA), which the principal cancer therapeutic agent, is a nanoparticle formed by the high-pressure vibrations of paclitaxel and human albumin. It increases therapeutic efficacy by improving the enrichment efficiency of paclitaxel in tumor cells. It outperforms conventional paclitaxel in terms of the full remission rate and overall survival in patients with early stage breast cancer and lung squamous cell carcinoma who received neoadjuvant therapy.<sup>5</sup> However, the overall treatment effect remains non-ideal, and the safety of the treatment, which may be related to systemic toxicity caused by PA, clearance of nano-drugs by the reticuloendothelial and complement systems, tumor accumulation, and insufficient penetration, must be improved. Therefore, designing and developing drug delivery techniques that limit systemic toxicity while improving tumor targeting can improve the therapeutic efficacy and survival status of patients with breast cancer.

Extracellular vesicles (EVs) are phospholipid bilayer-enclosed vesicles found in tissue culture supernatants and biological fluids that are secreted by all cell types. EVs are made up of a diverse population of particles that are classified as exosomes, microvesicles, or apoptotic bodies based on their biogenesis.<sup>6</sup> Exosomes are generated by the inward budding of the nucleosome's limiting membrane, which forms multivesicular bodies that are then joined with the plasma membrane and discharged into the extracellular space. Exosomes can interact with extracellular matrix or produce a response in the microenvironment or distant cells after being released from the cell surface. CD63 is an exosome-specific marker. Microvesicles are a kind of EVs formed by direct budding of the plasma membrane. Apoptotic bodies are also generated on the cell surface, but exclusively by apoptotic cells, and Annexin V is the particular marker for them. Exosomes are 40–120 nm in size, microvesicles are 50–1000 nm in size, and apoptotic bodies are 500–1000 nm in size.<sup>7,8</sup> They overlap in size. EVs separated by differential centrifugation are not, strictly speaking, vesicles. Tumor cell-derived vesicles transporting various hydrophobic and hydrophilic

<sup>1</sup>Center of Gene Sequencing, Shanxi Bethune Hospital, Shanxi Academy of Medical Sciences, Tongji Shanxi Hospital, Third Hospital of Shanxi Medical University, Taiyuan 030032, P.R. China

<sup>2</sup>Shanxi Bethune Hospital, Shanxi Academy of Medical Sciences, Tongji Shanxi Hospital, Third Hospital of Shanxi Medical University, Taiyuan 030032, P.R. China

<sup>3</sup>Department of Epidemiology, School of Public Health, Shanxi Medical University, Taiyuan 030001, P.R. China

<sup>4</sup>Department of Pathology & Shanxi Key Laboratory of Carcinogenesis and Translational Research of Esophageal Cancer, Shanxi Medical University, Taiyuan, Shanxi 030001, P.R. China

<sup>5</sup>Shanxi Academy of Advanced Research and Innovation, Taiyuan 030032, China

<sup>6</sup>Shanxi Jinzhong Health School, Jinzhong 030600, P.R. China

<sup>7</sup>The Radiology Department of Shanxi Provincial People's Hospital, The Fifth Hospital of Shanxi Medical University, Taiyuan 030001, P.R. China

<sup>8</sup>These authors contributed equally

<sup>9</sup>Lead contact

\*Correspondence: [zrp\\_7142@sxmu.edu.cn](mailto:zrp_7142@sxmu.edu.cn)

<https://doi.org/10.1016/j.isci.2024.108833>



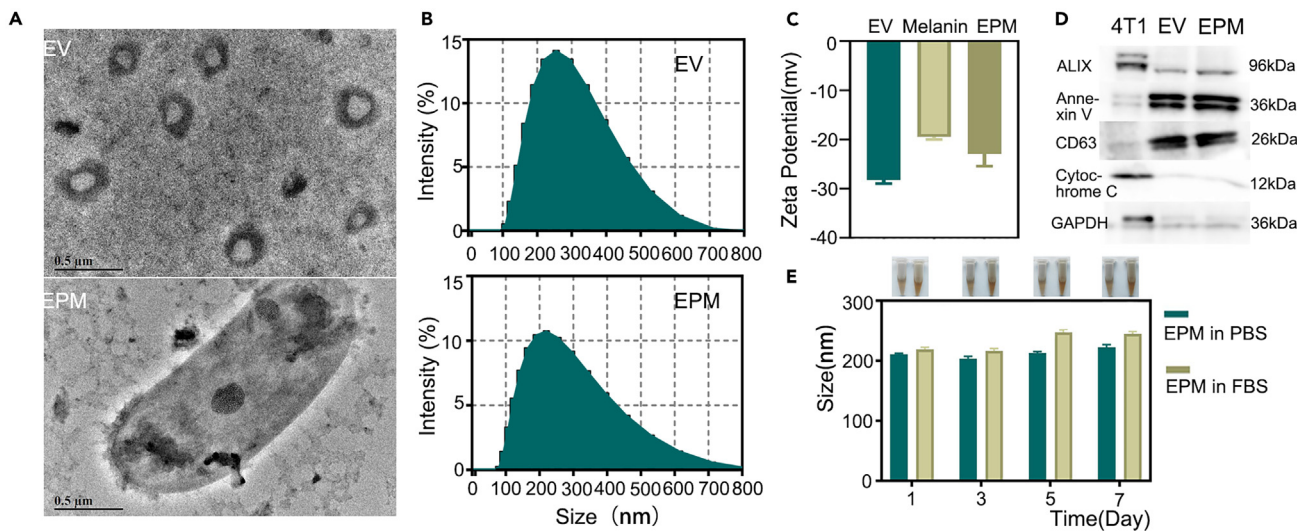


**Figure 1. Characterization of EPM**

(A) TEM images of EVs and EPM. Scale bars, 0.5  $\mu\text{m}$ .

(B) Overall distribution of hydrodynamic diameters of EVs and EPM (DLS).

(C) Zeta potential of EVs, melanin, EPM.

(D) The protein expression of CD63, ALIX cytochrome c, and Annexin V in EVs, EPM, and 4T1 cells.

(E) Stability analysis of EPM: average hydrodynamic diameter of EPM.

drugs can be employed as nanocarriers for cell communication and tumor-targeted therapies.<sup>9,10</sup> They exhibit favorable stability, biocompatibility, extended blood circulation, and tumor tissue targeting, which can stimulate the immune system to induce specific immune responses.<sup>11–14</sup> EVs loaded with chemotherapeutic drugs are promising for novel drug delivery applications. Targeted delivery may increase the uptake of chemotherapeutic drug-loaded vesicles by cancer cells and improve their killing efficiency. In recent years, the development of multifunctional nanomaterials that can incorporate numerous therapeutic modalities into a single nanoplatform has progressed significantly. In most cases, the combination of multiple medicines yields better therapeutic effects than employing a single therapy.<sup>15–18</sup> Chemotherapy combined with photothermal therapy (PTT) has received public interest. This synergistic treatment method not only retains the advantages of PTT, such as its noninvasive nature, low toxicity, and ease of administration, but also solves the problems of nonselectivity and multidrug resistance presented by conventional chemotherapy. Preclinical studies of several cancers have shown promising therapeutic effects.<sup>18,19</sup> The photothermal agent used for PTT critical. Currently, most photothermal agents investigated are inorganic nanoparticles (such as gold, carbon, palladium, and magnetic nanoparticles), near-infrared (NIR) dyes (polycyano green and IR825), polymer nanoparticles (such as polydopamine, polyaniline, polypyrrole, and poly [ethylthiophene]), and other nanomaterials (such as porous bodies and Prussian blue).<sup>20</sup> However, problems such as long-term *in vivo* safety, insufficient tumor tissue targeting, and retention have prevented its clinical application.

Melanin is an abundant pigment present in living organisms that exhibits excellent biocompatibility and photothermal conversion efficiency. It can transform light energy into heat energy and photoacoustic signals, which can simultaneously satisfy the demands of tumor treatment and imaging owing to its high absorption in the visible and NIR light regions.<sup>21</sup> Herein, we present a straightforward incubation procedure for creating a melanin and PA-loaded vesicle nanosystem. Based on an enhanced penetration retention (EPR) effect, the nanosystem can passively reach the tumor location, whereas tumor cell-derived EVs can aggressively target cancer cells. To achieve a precise and synergistic treatment of breast cancer, the immune system is stimulated to release PA and melanin. In fact, the released melanin can be used for the photoacoustic imaging and PTT of tumor tissues.

## RESULTS

### Preparation and characterization of EPM

EVs were generated after the ultraviolet irradiation of 4T1 cells at room temperature. The EPM was created by co-extruding EV, PA, and melanin through a 200 nm porous polycarbonate membrane. Transmission electron microscopy (TEM) and nanoparticle tracking analysis (NTA) were performed to examine the size, shape, and zeta potential of the EVs and EPM, respectively. TEM results show that the EVs and EPM were spherical, with a comparable diameter and size of 128 nm (Figure 1A). Based on the NTA, the average particle size of EVs was 129.5 nm, and the mode was 255 nm, whereas the average particle size of EPM was 113.9 nm, and the mode is 220 nm (Figure 1B). These results indicate that melanin and PA loading resulted in a modest increase in the EVs size. This size range permits efficient bodywide circulation and accumulation at the tumor location. Moreover, the electronegative melanin was effectively loaded, as reflected by the slight change in the zeta potential of EV-loaded melanin, that is, a decrease from  $-24.8$  to  $-28.5$  mV (Figure 1C). Using high-performance liquid

**Table 1. Encapsulation efficiency of paclitaxel and MNP in EPM**

Mass ratio of EV to PA and MNP(EV/PA and MNP)	Encapsulation efficiency of paclitaxel in EPM(%)	Encapsulation efficiency of MNP in EPM(%)
1mg EV : 39mg PA and 1mg MNP	48.59%	49.58%
1mg EV : 59mg PA and 1mg MNP	85.80%	39.68%
1mg EV : 79mg PA and 1mg MNP	91.51%	31.73%
1mg EV : 99mg PA and 1mg MNP	86.08%	24.29%
1mg EV :119mg PA and 1mg MNP	82.02%	23.66%

chromatography (HPLC), we confirmed that the Paclitaxel loaded 91.51% and melanin loaded 31.73% in EPM (Table 1). In addition, western blotting was performed to detect the expression of EVs markers to determine the effects of drug loading and melanin on the EVs characteristics. Whereas vesicle transport-related proteins ALIX and cytochrome c (mitochondrial markers) were only detected in cell lysates, Annexin V and CD63 were only detected in the EV and EPM (Figure 1D).

Maintaining colloidal stability is essential for the therapeutic use of drug carriers. We continuously monitored the particle size change and dispersion of EVs and EPM in PBS and 10% FBS for 1 week. Its polydispersity index was 0.304, and its average hydrodynamic diameter was approximately 211.87 nm. The stability and dispersibility of the EPM were favorable (Figure 1E), thus suggesting that its high colloidal stability in biological media might increase its anticancer activity *in vivo* and extend its blood circulation time.

### Photoacoustic and photothermal heating (PTT) efficiency of EPM

Melanin is promising not only for disease detection, but also for treatment. Through photothermal ablation or therapy, irradiated melanin triggers local heating and destroys pathological tissues. Therefore, we investigated whether EPM-loaded melanin generates a photoacoustic signal. Figure 2A shows that the photoacoustic signal of the EPM solution was approximately 239.65 times stronger than that of EVs under 808 nm laser irradiation. To clarify the potential of the EPM as a nanoheater for PTT, we monitored the real-time infrared thermal image and temperature change of a series of EPM solution concentrations (0, 12.5, 25, 50, 100, and 200  $\mu\text{g}/\text{mL}$ ) for 5 min. The temperature of the 200  $\mu\text{g}/\text{mL}$  EPM solution reached 76.3°C, thus indicating that melanin underwent efficient photothermal conversion. By contrast, the temperature of DI water increased to only 34.2°C (Figure 2C), thus confirming that the photothermal conversion was caused by the EPM. Increasing the temperature of the EPM solution is highly correlated with increasing the concentration (Figure 2B). Furthermore, the temperature of the EPM solution (100  $\mu\text{g}/\text{mL}$ ) increased to 71.4°C after 1.0  $\text{W}/\text{cm}^2$  of irradiation, which was greater than those achieved under irradiances of 0.25, 0.5, and 0.75  $\text{W}/\text{cm}^2$  (Figures 3D and 3E). Another important parameter for evaluating photothermal agents is their photothermal stability. Thus, we analyzed the heating and cooling curves of 100  $\mu\text{g}/\text{mL}$  EPM after 15 min of continuous laser irradiation (Figure 2F). To evaluate thermo-cycling, we exposed the EPM solution to an 808 nm laser with a power of 0.5  $\text{W}/\text{cm}^2$  (Figure 2G). The EPM showed acceptable photothermal stability after seven continuous closure/opening laser cycles and is thus potentially applicable for killing tumor cells.

### Anti-tumor effect *in vitro*

To determine the efficacy of the EPM in killing tumor cells, we first labeled EVs with the fluorescent dye, Dir, and co-incubated them with 4T1 cells for 0.5 h, 1 h, and 3 h, separately. Using flow cytometry, we discovered that the uptake of EPM-Dir by 4T1 cells increased in a time-dependent manner. The uptake rate of EPM-Dir was 84.1% after 1 h and 99.1% after 3 h (Figure 3A), which is consistent with the confocal imaging results. The uptake of EPM-Dil by 4T1 cells was approximately 100% after 3 h of co-incubation (Figure 3B). A standard endocytosis inhibitor was used to investigate the internalization mechanism of EPM into 4T1 cells. Based on the results, the uptake efficiency of EPM-Dir/EPM-GFP by 4T1 cells at 4°C was lower than that at 37°C ( $p < 0.001$ ), thus indicating that the internalization process of the EPM was energy driven. Furthermore, the uptake rate of the chlorpromazine group was considerably lower than that of the control group ( $p < 0.001$ ). However, amiloride did not affect the uptake efficiency, thus indicating that EPM endocytosis was primarily mediated by lectin and independent of the macrophage pathway (Figures 3C and S1).

Subsequently, we added EPM (containing 100  $\mu\text{g}/\text{L}$  of PA)/EM to the 4T1 cells, with free PA serving as a control to observe their effect on cell apoptosis. The EPM group contained 71.6% apoptotic cells, which showed a greater pro-apoptotic impact than free PA. After 808nm laser irradiation, the proportion of apoptotic cells in the EPM group was 87.7%, which were substantially greater than in the free PA and EPM unirradiated groups. As a result, EPM may enhance the therapeutic efficacy of chemotherapy and photothermal treatment in cancer patients (Figures 3D and 3E).

### Anti-tumor effect *in vivo*

To further illustrate EPM's exceptional efficacy in tumor treatment, we employed an orthotopic breast cancer mouse model to assess the efficacy of image-guided PTT for tumor treatment *in vivo* based on the superior imaging and photothermal conversion capabilities of the EPM. We randomly assigned orthotopic breast cancer mice into seven groups: PBS, PBS + Laser, PA, EM, EM + Laser, EPM, EPM + Laser group, and injected 50  $\mu\text{L}$  PBS or EPM (PA 30  $\text{mg}/\text{mL}$ ) around the tumor. Based on photoacoustic imaging data, the maximum concentration of EPM was observed at the tumor site 4 to 8 h after injection (Figures 4A and 4B). Therefore, the mice were exposed to an 808 nm laser for 5 min 4 h after

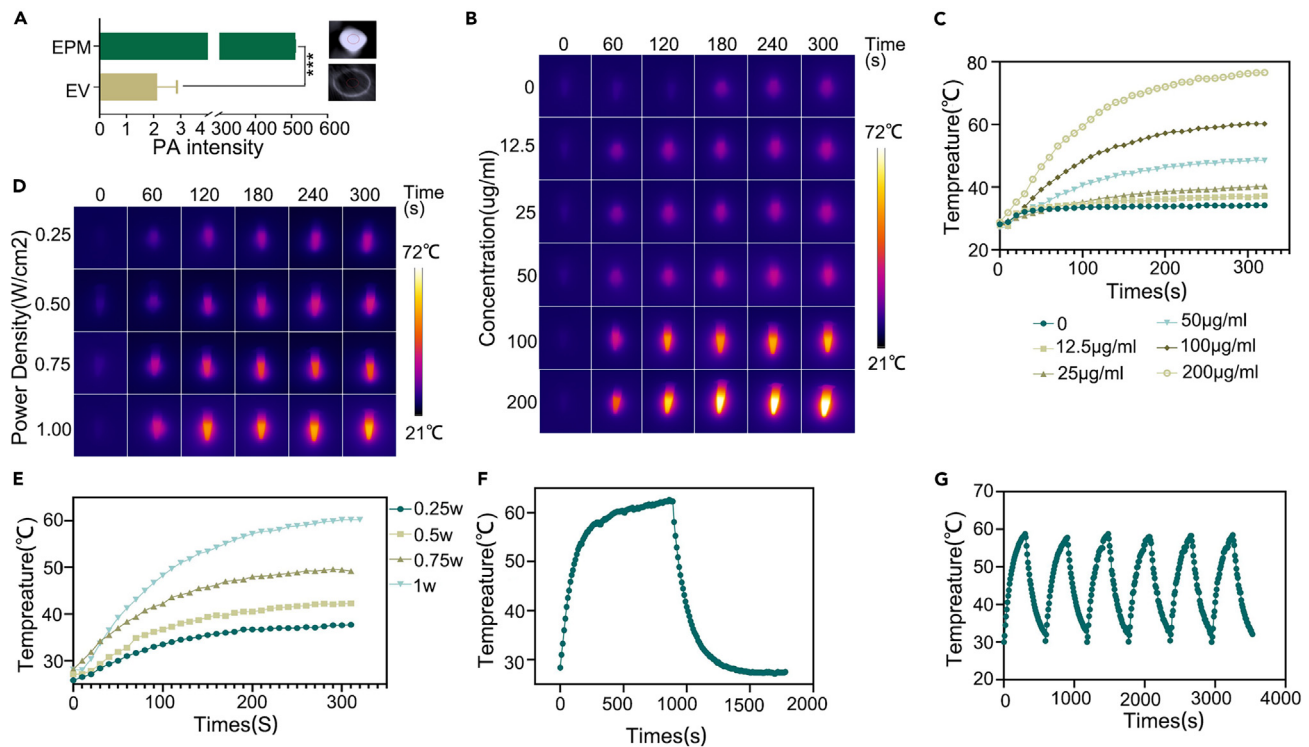


**Figure 2. Evaluation of photoacoustic, photothermal performance of EPM**

(A) Photoacoustic signal of EPM and EVs solution. Data are represented as mean  $\pm$  SEM. \*\*\*  $p < 0.001$ .  
 (B) Concentration-dependent thermal infrared images of EPM solutions within 5 min under 808 nm laser irradiation ( $1 \text{ W/cm}^2$ ).  
 (C) Temperature change curves of a series of EPM solutions with different concentrations recorded with 808 nm laser irradiation ( $1 \text{ W/cm}^2$ ).  
 (D) Power density-dependent thermal infrared images of EPM solutions ( $100 \mu\text{g/mL}$ ) within 5 min under 808 nm laser irradiation.  
 (E) Temperature change curves of EPM solution ( $100 \mu\text{g/mL}$ ) under 808 nm laser irradiation with different power densities.  
 (F) The heating and cooling curves of EPM solution ( $100 \mu\text{g/mL}$ ) measured with irradiation of 808 nm laser ( $1 \text{ W/cm}^2$ ).  
 (G) Photothermal stability of EPM ( $100 \mu\text{g/mL}$ ) solution upon irradiation for six cycles (808 nm,  $1 \text{ W/cm}^2$ ).

injection. The tumor volume and body weight of 4T1 tumor-bearing nude mice were monitored continuously. The mice were sacrificed 24 days after inoculation, and the tumors were removed to assess the therapeutic efficacy (Figure 4C). The tumor volumes of the four groups (PBS, PBS + Laser, PA, and EM groups) increased over time, particularly in the final stages. By contrast, tumors in the EPM + laser treatment group showed considerable tumor growth inhibition in the first four days and no recurrence over the entire observation period (Figures 4D and 4E). In addition, no significant change in body weight was indicated between the EPM and EPM + laser groups, thus indicating that EPM-mediated local tumor photothermal ablation was not associated with any deleterious effects (Figure 4F). To further understand the systemic toxicity of the EPM *in vivo*, we obtained blood and major organs (heart, liver, spleen, lungs, and kidneys) from healthy mice following a high-dose injection of EPM. Hematological examination revealed no signs of acute toxicity in the liver (alanine aminotransferase, ALT, and serum aspartate aminotransferase, AST) and kidney (serum creatinine, Scr, and blood urea nitrogen, BUN). Hematoxylin and eosin (H&E) staining of tissue slices in the EPM group revealed no evident necrosis, apoptosis, or other pathological changes in the main organs compared with those in the PBS group (Figure 4K). Furthermore, we injected the orthotopic breast cancer mouse model through the tail vein with Dir-labeled EPM. The fluorescence imaging results revealed that the fluorescence signal of EPM appeared in the tumor tissue 2 h after injection and disappeared 10 h later, whereas the fluorescence signal appeared in the liver 1 h after injection, then gradually attenuated, and completely metabolized at 4 h. Other organs showed no noticeable fluorescence signal. Only a modest fluorescence signal was discovered in the liver after 48 h of continuous monitoring, whereas other tissues and organs were observed (Figure S2). These findings indicate that the EPM exhibits high biocompatibility and negligible systemic toxicity *in vivo*.

### Activation of immune response by EPM

Based on the previous results, the EPM exhibited significant inhibitory effect on tumors compared with EM and PA. EVs generated from tumor cells may stimulate immunological responses, in addition to facilitating tumor targeting. Therefore, we hypothesized that the superior anti-tumor efficacy of EPM is due to the synergistic effects of immunotherapy, chemotherapy, and photothermal treatment. To test this hypothesis, we examined the effect of the EPM on immune response by identifying immune cells *in vitro* and *in vivo*.

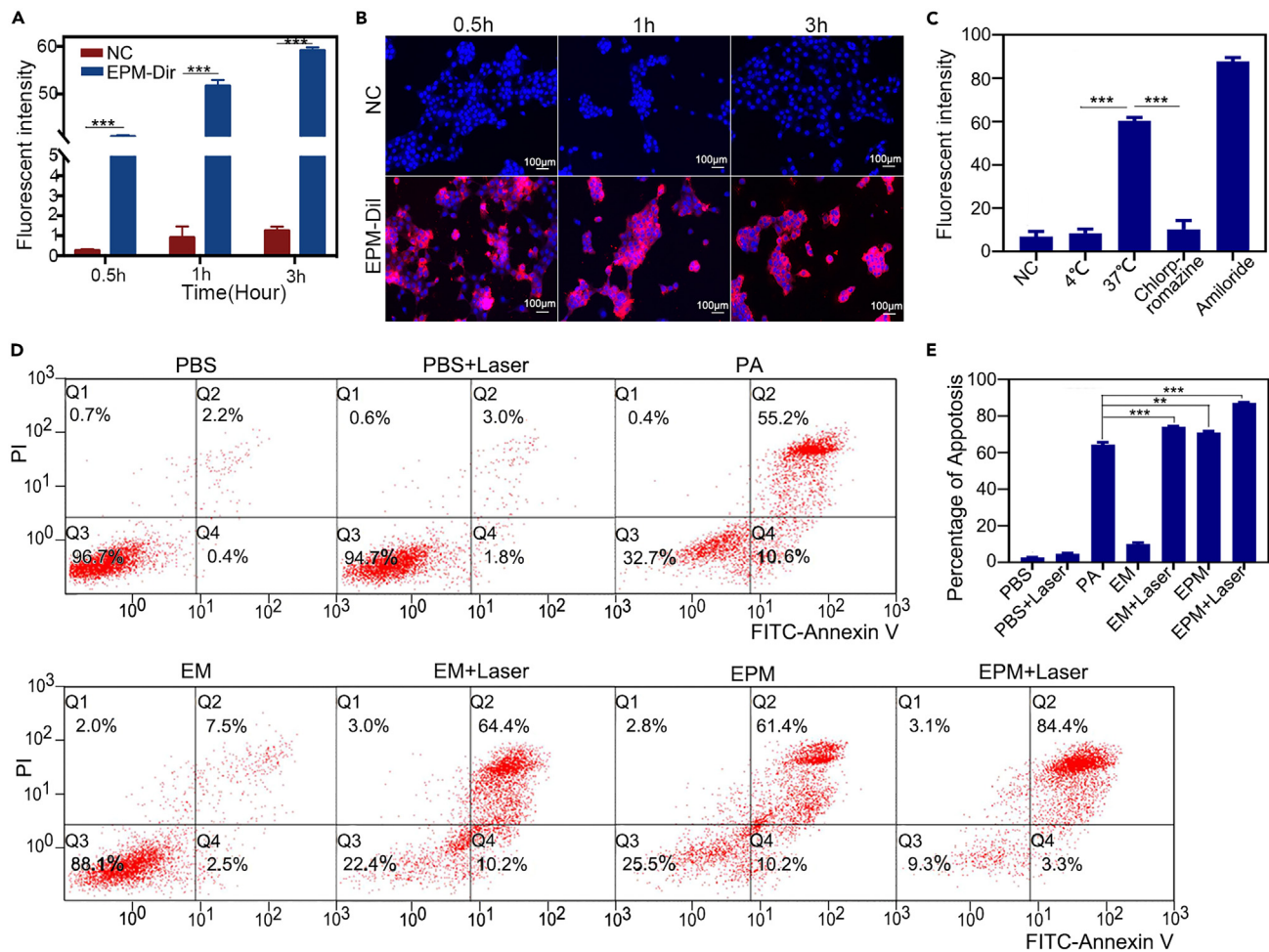


**Figure 3. EPM uptake by 4T1 cells, evaluation of internalization mechanism, and EPM lethal impact on 4T1 cells**

(A) Flow cytometry was used to quantify 4T1 cell EPM uptake at 0.5 h, 1.0 h, and 3 h.

(B) Laser confocal images of 4T1 cells uptake EPM at the above time points. Orange-red fluorescence represents Dir-labeled EPM, blue fluorescence (DAPI) represents cell nuclei, and the merge image shows the combination of orange-red and blue fluorescence. Scale bar, 100  $\mu$ m. Data are represented as mean  $\pm$  SEM. \*\*\* $p$  < 0.001.

(C) Flow cytometry was used to quantify 4T1 cell EPM uptake under different conditions, including 4°C, 37°C, chlorpromazine (100  $\mu$ M), and amiloride hydrochloride (25  $\mu$ M). Data are represented as mean  $\pm$  SEM. \*\*\* $p$  < 0.001.

(D and E) Flow cytometry was used to detect the effect of EPM on 4T1 cell apoptosis. \*\* $p$  < 0.01, \*\*\* $p$  < 0.001.

Antigen-specific immune cells activated by antigen-presenting cells (APCs) are used in tumor immunotherapy. Dendritic cells (DCs), which is a type of APC, are key to the stimulation and regulation of innate and adaptive immunity. It should be emphasized that only mature DCs have the function of antigen presentation. And the expression of co-stimulatory molecules (CD80 and CD86) can be used to estimate the maturity of DCs. Hence, we isolated immature DC cells from C57BL/6J mice (4 week old) bone marrow for culture. On the eighth day of DCs culture, we replaced the medium containing GM-CSGF and IL-4 with conditioned medium created by the EPM and 4T1 co-incubation and continued to grow it for 12 h to better understand the effect of the EPM on DCs maturation. Flow cytometry data showed that the maturation rate of DCs (CD80<sup>+</sup>CD86<sup>+</sup>) in the EPM group was 50.7%, which was twice that of PBS group, suggesting that EPM promoted DCs maturation (Figures 5A, 5B, and S3A–S3C). In addition, flow cytometry was also used to assess the efficiency of EPM absorption by mature DCs. After 3 h, the absorption efficiency of EPM by CD80<sup>+</sup>CD86<sup>+</sup> DCs reached approximately 100% (Figures 5C and S3A–S3C). This suggests that mature DCs have a high affinity for EPM, which underpins their tumor immune response.

Subsequently, to confirm that EPM does initiate a specific immune response, we examined the infiltrating T cells in mouse tumor tissues to clarify the DCs-mediated immune response. The number of CD3<sup>+</sup>CD8<sup>+</sup> T cells in the tumors of the EPM and EPM + Laser group was 6.3% and 11.2%, which significantly higher than that in the tumors of the free PA group. Simultaneously, the number of CD3<sup>+</sup>CD8<sup>+</sup> T cells in tumors of mice treated with tumor cell derived vesicles was higher than in the non-containing groups (Figures 5D, 5E, and S3D–S3G). These findings indicate that EPM can successfully boost the immune system in mice, paving the way for synergistic chemotherapy, PTT, and immunotherapy.

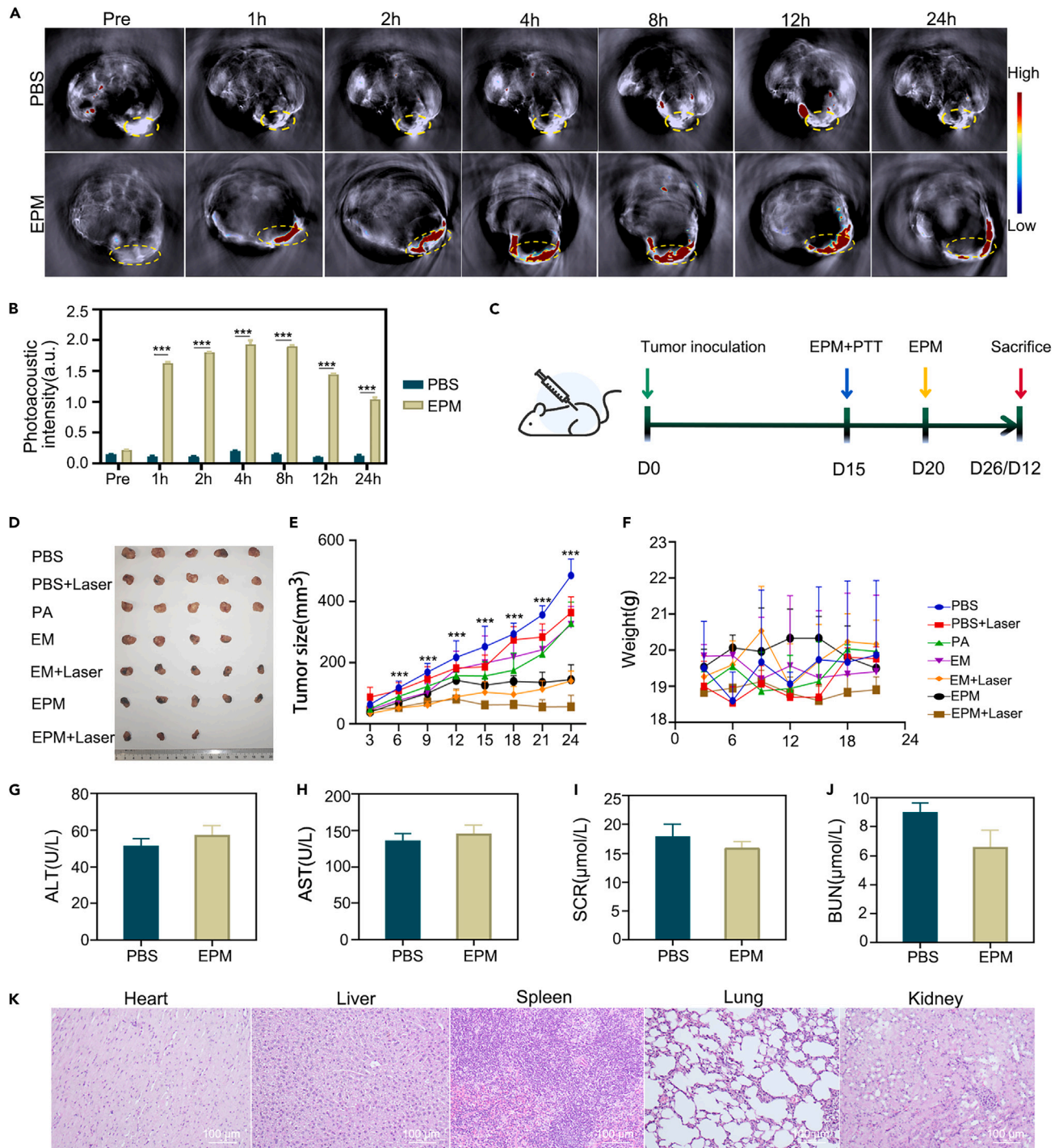


**Figure 4. In vivo imaging and evaluation of therapeutic effect**

(A) Representative time-dependent photoacoustic images in orthotopic breast cancer mice treated with EPM at predetermined time points during 24 h. (B) The quantitative analysis intensities of tumor tissue (n = 3) determined by photoacoustic imaging at selected time intervals. Data are represented as mean ± SEM. \*\*\*p < 0.001.

(C) Schematic depicting the experimental approach.

(D) Photographs of excised tumors (n = 5 per group) at day 26 after different treatments.

(E) Relative tumors growth curves (n = 5 per group). p values were obtained using ANOVA. \*\*\*p < 0.001 by Student's t test.

(F) Body weight curves (n = 5 per group).

(G–J) Detection of biomarkers of liver (ALT and AST) and kidney function (Scr and BUN) in mice (n = 3) with high-dose EPM injection.

(K) Representative pictures of H&E staining of major organ tissues in mice with high-dose EPM injection. Scale bar, 100 μm.

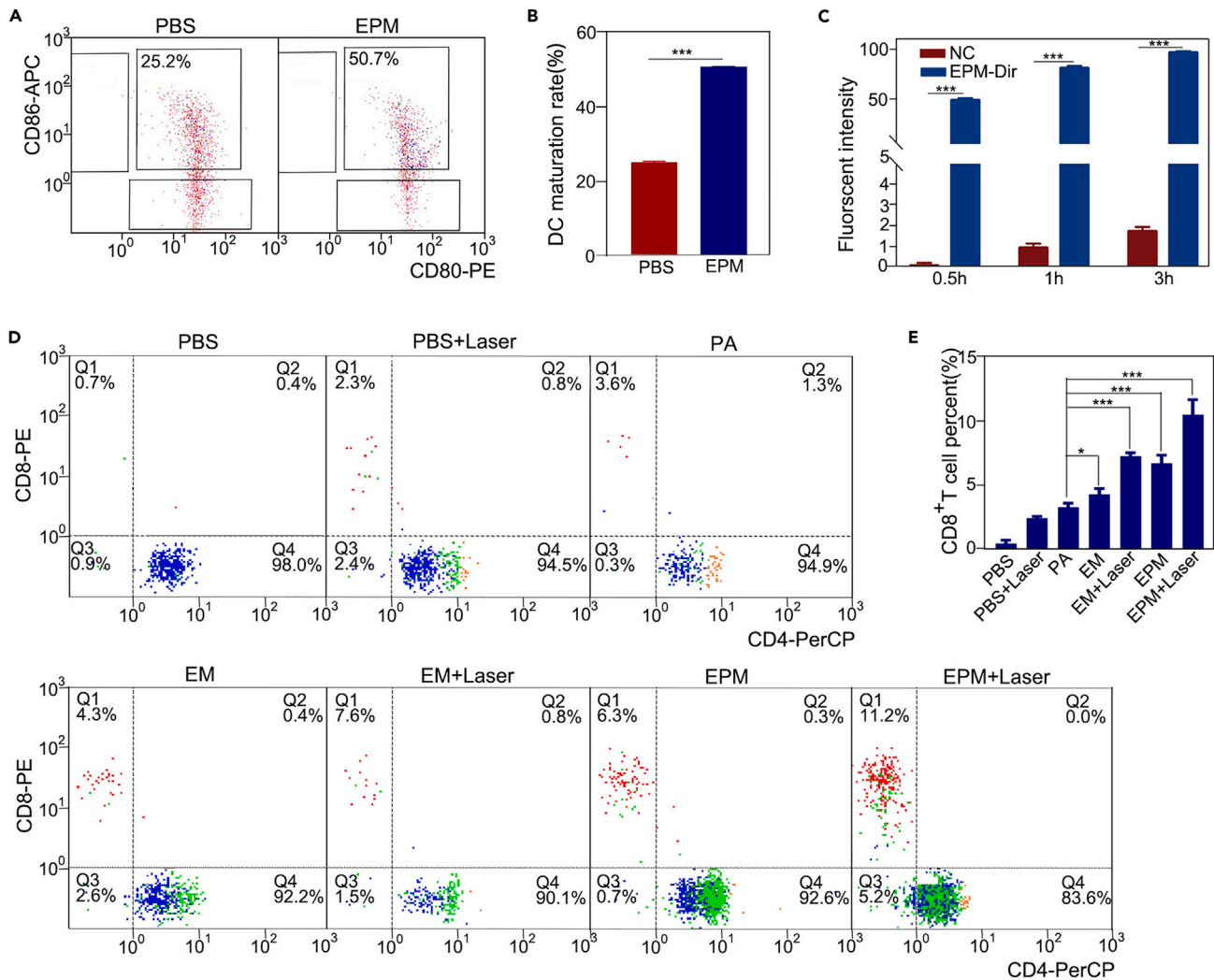


**Figure 5. Evaluation of immune effects of EPM**

(A and B) The proportion of CD80 and CD86 double-positive cells in CD11c<sup>+</sup> DCs was detected by flow cytometry. Data are represented as mean  $\pm$  SEM. \*\*\**p* < 0.001.

(C) Assessment of EPM uptake by macrophages. Flow cytometry was used to quantify by CD80<sup>+</sup>CD86<sup>+</sup> DCs EPM uptake at 0.5 h, 1.0 h, and 3 h. Data are represented as mean  $\pm$  SEM. \*\*\**p* < 0.001.

(D and E) Flow cytometry was used to detect CD3<sup>+</sup>CD8<sup>+</sup> T cell infiltration in tumor tissues (*n* = 5 per group). Data are represented as mean  $\pm$  SEM. \**p* < 0.05, \*\*\**p* < 0.001.

## DISCUSSION

Currently, researchers have conducted several studies combining immunotherapy with chemotherapy, PTT, photodynamic therapy, and other ways in order to achieve the complimentary benefits and functional amplification of multiple therapeutic modalities. Multimodal combination therapy has been shown to be an effective strategy for the treatment of cancer. PTT, which is minimally invasive, controlled, efficient, and specialized, can effectively compensate for the toxicity, adverse effects, and tumor drug resistance associated with conventional drug therapy.<sup>22</sup> Studies showed that the combination of PTT and chemotherapy presented a synergistic antitumor effect.<sup>23,24</sup> However, chemotherapeutic and photothermal agents may exhibit distinct pharmacokinetic characteristics *in vivo*, thus rendering it difficult to ensure adequate transmission at the tumor site. Furthermore, additional problems must be considered, such as the rapid metabolism and degradation of the free form in the body. A critical challenge in combination antitumor applications is the efficient and synchronous delivery of drugs/photothermal reagents from multiple therapy modalities to tumor tissues to achieve the optimal antitumor effect. However, EVs offer distinct benefits as drug delivery carriers.<sup>8,25,26</sup> They are generated from cells and contain membrane proteins, RNA, DNA, and other donor-cell components. They can transport these bioactive chemicals as well as exhibit tissue-specific homing effects.<sup>6</sup>

EVs are membrane-structured vesicles secreted by cells. They are classified into three divisions based on their sizes and modes of occurrence: exosomes (30–150 nm), microvesicles (50–1000 nm), and apoptotic bodies (100–5000 nm).<sup>8</sup> Although their diameters and manufacturing techniques differ, their research and application directions are comparable, with the majority of their applications being in tissue healing, damage repair, diabetes, myocardial infarction, anti-tumor, and other disciplines. Apoptotic bodies are vesicular entities created during the apoptosis process by shrinking and invaginating the cell membrane and splitting and enveloping the cytoplasm. Apoptotic cells may make apoptotic bodies more efficiently than live cells, and the process of apoptosis can be totally controlled by standardized operation.<sup>7,27</sup> As a result, interest in apoptotic bodies has grown steadily in recent years. The study of Zhao proposed that apoptotic bodies can transport residual medicines to nearby tumor cells following apoptosis.<sup>28</sup> Wang's research results show that nano-scale apoptotic bodies released by brain metastatic cancer cells can be employed as a medication delivery carrier capable of crossing the blood-brain barrier.<sup>29</sup> And EVs from various sources can be employed as drug carriers. For instance, red blood cell membrane were natural, abundant and safe, and can be used as a favorable antitumor tool after being endowed with target ability.<sup>30</sup> Gong et al. loaded doxorubicin (Dox) into poly(lactic-co-glycolic acid) (PLGA) NPs and coated them with a hybrid coating of macrophage (RAW264.7) membranes and breast cancer cell (4T1) membranes to form new biomimetic nanocarriers to target homologous cancer cells, efficiently track the tumor and kill the tumor tissue.<sup>31</sup> Stem cell EVs contain stem cell-specific reprogramming factors with antitumor function that reprogram malignant tumors to a benign phenotype.<sup>32</sup> Conjugated cationic bovine serum albumin and siS100A4 and then encapsulated them within autologous breast cancer-derived exosomes to form a novel biomimetic carrier.<sup>33</sup> Thankfully, tumor cells have five times the capacity of normal cells to take up tumor cell-derived vesicles.<sup>34</sup> In addition, unlike normal tissue blood vessels, tumor tissue blood vessels are not formed well, with a vascular endothelial gap of 100–780 nm and tumor vesicles measuring 200–500 nm on average.<sup>35–37</sup> Therefore, tumor-derived vesicles cannot enter normal tissue but can enter tumor tissue. Moreover, tumor-derived EVs are chemotactic to tumor-adjacent lymph nodes, induce an effective T cell immune response, form a strong antitumor immune response, and monitor and kill residual tumor cells long-term by activating specific antitumor immune effects.<sup>13,34</sup>

In recent years, significant progress has been achieved in the development of multifunctional nanomaterials based on tumor EVs that can integrate various therapy approaches into a single nanoplatform. In most cases, the combination of various medicines outperforms single therapy in terms of therapeutic impact. For tumor treatment research, therapeutic medicines and photosensitizers are primarily loaded into tumor EVs by incubation, extrusion, electroporation, ultrasound, and gene editing. Intrapleural injection of cisplatin-loaded vesicles derived from A549 human lung cancer cells dramatically decreased the total number of cancer cells in pleural effusion of three patients with cisplatin-resistant end-stage lung cancer in a clinical investigation.<sup>38</sup> Wu et al. developed tumor EVs nanoparticles based on tumor immunotherapy, which created tumor *in situ* vaccine by triggering tumor cell death, employing the homotypic targeting capacity of tumor EVs to transport DOX.<sup>39</sup> Wang employed tumor EVs to encapsulate the photosensitizer Ce6 in nanoparticles formed by ovalbumin. The ROS produced by the photosensitizer after illumination dramatically increased the efficiency of antigen cross-presentation, potentially initiating the immunological cascade reaction and improving the efficacy of standard photodynamic treatment.<sup>40</sup> Zheng et al. incubate tumor cells with gold nanorods linked to CpG before exposing them to UV light to create apoptotic bodies laden with gold nanorods. The photothermal action induced by gold nanorods under NIR light irradiation successfully kills the tumor.<sup>41</sup>

PA is a nano-drug that is used to treat cancer. Patients with early breast cancer neoadjuvant treatment and lung squamous cell carcinoma had a higher rate of full remission and overall survival than with standard paclitaxel.<sup>5</sup> In comparison to paclitaxel, albumin is an endogenous product of the human body. It can employ the albumin receptor Gp60 on the cell membrane and the role of cysteine-rich acidic secretory protein (SPARC) in tumor tissue to improve drug entry and increase chemotherapy efficacy.<sup>42</sup> However, the total therapeutic impact in clinical application is still not optimum. Melanin, as a natural photosensitizer, may be used to accomplish multimodal imaging and tumor therapy by various surface alterations.<sup>43</sup> Jiang<sup>44,45</sup> demonstrated that nanoparticles made of simple red cell membrane or red cell-cancer hybrid membrane coated with melanin can boost tumor photothermal treatment effectiveness. Gujrati stated that melanin-encapsulated bioengineered bacterial vesicles have the potential for image enhancement and photothermal applications.<sup>46</sup>

As a result, we proposed for the first time in this study to use tumor EVs to encapsulate PA and melanin to create a new nanomedicine for the treatment of orthotopic breast cancer via a combination of chemotherapy, photothermal, and immunotherapy. TEM showed no significant differences in the morphology and size of drug-loaded EVs and empty EVs. The shape of those vesicles was spherical and their size remained at 200nm, which is consistent with earlier bioengineering results.<sup>47</sup> Moreover, the EPM showed strong dispersibility and stability in serum, thus allowing it to remain in the bloodstream for an extended duration, which is conducive to passive accumulation in tumor tissues via the EPR effect. When the temperature of the EPM suspension increased to beyond 45°C within 2 min of NIR laser irradiation, cancer cells were killed, despite the fact that the body temperature is approximately 37°C. Additionally, the EPM in the tumor tissue was heated rapidly to beyond 45°C under NIR irradiation. To understand the lethal effect of the EPM on tumor cells, we first measured the EPM uptake by tumor cells. Flow cytometry and confocal microscopy data revealed that after 3 h of co-incubation with the EPM, the tumor cell uptake efficiency was approximately 100%, with considerable time dependence. Apoptotic cells were detected using flow cytometry, and the proportion of apoptotic cells in the EPM and PA groups was much greater than that in the control group. Several apoptotic effects were observed in the EPM group after laser irradiation, which is consistent with the high photothermal conversion efficiency of the EPM. Subsequently, we demonstrated the effectiveness of EPM photothermal treatment via *in vivo* experiments. The results showed that the EPM significantly reduced tumor volume growth in mice while minimally affecting mouse weight. The necrotic tissue of the EPM increased significantly in the H&E-stained sections of the tumor tissue, thus suggesting that the cytotoxicity of the EPM to tumor cells was more efficient than direct treatment with PA alone.

Studies showed that tumor antigen epitopes on the surface of tumor cells can be identified using CD8<sup>+</sup> and CD4<sup>+</sup> T cells. This not only induces an anti-tumor immune response and inhibits tumor escape, but also promotes DCs maturation and creates a favorable cytokine

environment.<sup>48–50</sup> Tumor cells contain various immunosuppressive signals that ensure a constant immunosuppressive tumor microenvironment.<sup>51,52</sup> Tumor cell-derived EVs are membrane-like structures formed by tumor cells. Does the immunoregulatory effect of loaded chemotherapeutic drugs affect the tumor microenvironment? Antigen-specific immune cells activated by APCs are used in tumor immunotherapy.<sup>12</sup> DCs, which is a type of APC, are key to the stimulation and regulation of innate and adaptive immunity. It should be emphasized that only mature DCs have the function of antigen presentation. Immature DCs communicate with antigen and phagocytize it. These antigens transform into peptides during their journey to adjacent lymph nodes. These immature DCs are then converted into mature DCs. They transmit the major histocompatibility complex peptide to T cell receptors upon arrival in the lymph nodes, eliciting a specific immunological response.<sup>53,54</sup> Hence, we isolated immature DCs from C57BL/6J mice (4 week old) bone marrow for culture. Subsequently, mature and activated DCs expose antigens to naive T cells, initiating a systemic anti-tumor immune response.<sup>55</sup> Cytotoxic T lymphocytes (CTLs) (CD3<sup>+</sup>CD8<sup>+</sup>T cells) can directly kill target cancer cells, while helper T cells (CD3<sup>+</sup>CD4<sup>+</sup>T cells) play a vital role in adaptive immune regulation. They secrete various immunomodulating factors to regulate the function of immune cells, achieving the suppression of tumors. Additionally, they can activate CTLs to kill tumor cells.<sup>56</sup> Therefore, we performed flow cytometry to examine the proportion of mature DCs and T cells in tumor tissues of mice. We discovered that the EPM promoted DCs maturation and increased CD3<sup>+</sup>CD8<sup>+</sup>T cell infiltration in tumor tissues, thus implying that the EPM may not only affect tumor treatment via encapsulated chemotherapeutic drugs, but also activate tumor immunity. Tumor cell-derived EVs may efficiently deliver chemotherapeutic drugs to tumor cells and cause tumor cell death. The complete release of tumor antigens triggers an immune response in the tumor microenvironment.

## Conclusion

In summary, by using simple incubation and extrusion, we created a nano-drug delivery system based on breast cancer EVs that incorporates natural thermosensitizer melanin and nano-chemotherapeutic drug PA. This nano-drug delivery system is capable of successfully targeting breast cancers while achieving synergistic anti-tumor effects of chemotherapy, photothermal treatment, and immunotherapy.

## Limitations of the study

EV loading technology has emerged as a prominent research area in the field of nanomedicine during the last few decades. People are attempting to convert the vesicle nanoplatform into a clinical platform as researchers continue to investigate. The EVs separation system cannot currently offer a pure population of certain EVs subtypes, and all research focus on the function of EVs mixtures. The preparation of EV using the differential centrifugation separation approach is either a heterogeneous population of tiny EVs or a combination of EVs of all sizes. As a result, further research is needed to determine when vesicles exhibit particularly significant physiological or pathological capabilities and to encourage them to become specific therapeutic targets or carriers. Furthermore, increasing manufacturing to a therapeutically appropriate number of vesicle nanoplatforms while maintaining tight quality standards is an application restriction to assure vesicle efficacy and safety. As a result, using endogenous homing features necessitates the separation of various EV subgroups with good transport characteristics, which is difficult with today's technology. Many issues must be addressed before EVs may be widely employed in clinical practice.

## STAR★METHODS

Detailed methods are provided in the online version of this paper and include the following:

- KEY RESOURCES TABLE
- RESOURCE AVAILABILITY
  - Lead contact
  - Materials availability
  - Data and code availability
- EXPERIMENTAL MODEL AND STUDY PARTICIPANT DETAILS
  - Animals and ethics statement
- METHOD DETAILS
  - Cell culture
  - Preparation of EPM
  - Transmission electron microscope (TEM) and dynamic light scattering (DLS)
  - High-Performance Liquid chromatography (HPLC)
  - Cell apoptosis
  - Flow cytometry and confocal microscopy
  - Western blot
  - Photothermal activity of EPM
  - Animal model
  - In-vivo photoacoustic imaging
  - Anti-tumor effect *in vivo*
  - In-vivo safety
  - Isolation of mouse immune cells

- Preparation of conditioned medium
- **QUANTIFICATION AND STATISTICAL ANALYSIS**

## SUPPLEMENTAL INFORMATION

Supplemental information can be found online at <https://doi.org/10.1016/j.isci.2024.108833>.

## ACKNOWLEDGMENTS

This work has been financially supported by the National Natural Science Foundation of China (no. 82120108016 and no. 82071987, no. 82002606), the National Key R&D Program of China (2023YFC3402800), Key Laboratory of Nano-imaging and Drug-loaded Preparation of Shanxi Province (no. 202104010910010), Shanxi Province “136 Revitalization Medical Project Construction Funds” (no.2021Y217). Science and Technology Innovation Project of Universities in Shanxi (no. 2021RC010). The Science and Technology Innovation Team of Shanxi Province (no. 202204051001024).

## AUTHOR CONTRIBUTIONS

R.Z. designed the experiments, supervised data analysis, and edited the manuscript. Y.B. and J.C. conceived the study and analyzed the data. Y.B., J.C., L.Z., and Y.L. performed experiments. Q.L. and Z.L. performed bioinformatics and statistics analyses. F.Y. and J.C. coordinated and performed pathology review. Y.B. wrote the manuscript. All authors had access to the study data and reviewed and approved the final manuscript.

## DECLARATION OF INTERESTS

The authors declare no competing interests.

Received: September 18, 2023

Revised: November 27, 2023

Accepted: January 3, 2024

Published: January 8, 2024

## REFERENCES

1. Pasha, N., and Turner, N.C. (2021). Understanding and overcoming tumor heterogeneity in metastatic breast cancer treatment. *Nat. Cancer* 2, 680–692. <https://doi.org/10.1038/s43018-021-00229-1>.
2. Riggio, A.I., Varley, K.E., and Welm, A.L. (2021). The lingering mysteries of metastatic recurrence in breast cancer. *Br. J. Cancer* 124, 13–26. <https://doi.org/10.1038/s41416-020-01161-4>.
3. Sun, Q., Bai, X., Sofias, A.M., van der Meel, R., Ruiz-Hernandez, E., Storm, G., Hennink, W.E., De Geest, B., Kiessling, F., Yu, H.-J., et al. (2020). Cancer nanomedicine meets immunotherapy: opportunities and challenges. *Acta Pharmacol. Sin.* 41, 954–958. <https://doi.org/10.1038/s41401-020-0448-9>.
4. Park, H., Otte, A., and Park, K. (2022). Evolution of drug delivery systems: From 1950 to 2020 and beyond. *J. Control. Release* 342, 53–65. <https://doi.org/10.1016/j.jconrel.2021.12.030>.
5. Bordeianu, G., Filip, N., Cernomaz, A., Veliceasa, B., Hurjui, L.L., Pinzariu, A.C., Pertea, M., Clim, A., Marinca, M.V., and Serban, I.L. (2023). The Usefulness of Nanotechnology in Improving the Prognosis of Lung Cancer. *Biomedicines* 11, 705. <https://doi.org/10.3390/biomedicines11030705>.
6. Elsharkasy, O.M., Nordin, J.Z., Hagey, D.W., de Jong, O.G., Schifflers, R.M., Andaloussi, S.E., and Vader, P. (2020). Extracellular vesicles as drug delivery systems: Why and how? *Adv. Drug Deliv. Rev.* 159, 332–343. <https://doi.org/10.1016/j.addr.2020.04.004>.
7. Tkach, M., Kowal, J., and Théry, C. (2018). Why the need and how to approach the functional diversity of extracellular vesicles. *Philos. Trans. R. Soc. Lond. B Biol. Sci.* 373, 20160479. <https://doi.org/10.1098/rstb.2016.0479>.
8. Walker, S., Busatto, S., Pham, A., Tian, M., Suh, A., Carson, K., Quintero, A., Lafrance, M., Malik, H., Santana, M.X., and Wolfram, J. (2019). Extracellular vesicle-based drug delivery systems for cancer treatment. *Theranostics* 9, 8001–8017. <https://doi.org/10.7150/thno.37097>.
9. Bose, R.J.C., Uday Kumar, S., Zeng, Y., Afjei, R., Robinson, E., Lau, K., Bermudez, A., Habte, F., Pitteri, S.J., Sinclair, R., et al. (2018). Tumor Cell-Derived Extracellular Vesicle-Coated Nanocarriers: An Efficient Theranostic Platform for the Cancer-Specific Delivery of Anti-miR-21 and Imaging Agents. *ACS Nano* 12, 10817–10832. <https://doi.org/10.1021/acsnano.8b02587>.
10. Li, A., Zhao, Y., Li, Y., Jiang, L., Gu, Y., and Liu, J. (2021). Cell-derived biomimetic nanocarriers for targeted cancer therapy: cell membranes and extracellular vesicles. *Drug Deliv. Rev.* 28, 1237–1255. <https://doi.org/10.1080/10717544.2021.1938757>.
11. Xu, J., Cao, W., Wang, P., and Liu, H. (2022). Tumor-Derived Membrane Vesicles: A Promising Tool for Personalized Immunotherapy. *Pharmaceuticals* 15, 876. <https://doi.org/10.3390/ph15070876>.
12. Marar, C., Starich, B., and Wirtz, D. (2021). Extracellular vesicles in immunomodulation and tumor progression. *Nat. Immunol.* 22, 560–570. <https://doi.org/10.1038/s41590-021-00899-0>.
13. Li, Q., Cai, S., Li, M., Salma, K.I., Zhou, X., Han, F., Chen, J., and Huyan, T. (2021). Tumor-Derived Extracellular Vesicles: Their Role in Immune Cells and Immunotherapy. *Int. J. Nanomedicine* 16, 5395–5409. <https://doi.org/10.2147/ijn.S313912>.
14. Xu, C., Ju, D., and Zhang, X. (2022). Cell Membrane-Derived Vesicle: A Novel Vehicle for Cancer Immunotherapy. *Front. Immunol.* 13, 923598. <https://doi.org/10.3389/fimmu.2022.923598>.
15. Sun, W., Sanderson, P.E., and Zheng, W. (2016). Drug combination therapy increases successful drug repositioning. *Drug Discov. Today* 21, 1189–1195. <https://doi.org/10.1016/j.drudis.2016.05.015>.
16. Zhu, S., Zhang, T., Zheng, L., Liu, H., Song, W., Liu, D., Li, Z., and Pan, C.-X. (2021). Combination strategies to maximize the benefits of cancer immunotherapy. *J. Hematol. Oncol.* 14, 156. <https://doi.org/10.1186/s13045-021-01164-5>.
17. Ayoub, N.M. (2021). Editorial: Novel Combination Therapies for the Treatment of Solid Cancers. *Front. Oncol.* 11, 708943. <https://doi.org/10.3389/fonc.2021.708943>.
18. Nam, J., Son, S., Ochyl, L.J., Kuai, R., Schwendeman, A., and Moon, J.J. (2018). Chemo-photothermal therapy combination elicits anti-tumor immunity against advanced metastatic cancer. *Nat. Commun.* 9, 1074. <https://doi.org/10.1038/s41467-018-03473-9>.
19. Li, X., Lovell, J.F., Yoon, J., and Chen, X. (2020). Clinical development and potential of photothermal and photodynamic therapies

- for cancer. *Nat. Rev. Clin. Oncol.* 17, 657–674. <https://doi.org/10.1038/s41571-020-0410-2>.
20. Wang, Y., Meng, H.-M., and Li, Z. (2021). Near-infrared inorganic nanomaterial-based nanosystems for photothermal therapy. *Nanoscale* 13, 8751–8772. <https://doi.org/10.1039/d1nr00323b>.
  21. Cordero, R.J.B., and Casadevall, A. (2020). Melanin. *Curr. Biol.* 30, R142–R143. <https://doi.org/10.1016/j.cub.2019.12.042>.
  22. Liu, X., Zhou, W., Wang, T., Miao, S., Lan, S., Wei, Z., Meng, Z., Dai, Q., and Fan, H. (2023). Highly localized, efficient, and rapid photothermal therapy using gold nanobipyramids for liver cancer cells triggered by femtosecond laser. *Sci. Rep.* 13, 3372. <https://doi.org/10.1038/s41598-023-30526-x>.
  23. He, P.P., Du, X., Cheng, Y., Gao, Q., Liu, C., Wang, X., Wei, Y., Yu, Q., and Guo, W. (2022). Thermal-Responsive MXene-DNA Hydrogel for Near-Infrared Light Triggered Localized Photothermal-Chemo Synergistic Cancer Therapy. *Small* 18, e2200263. <https://doi.org/10.1002/smll.202200263>.
  24. Chang, T., Qiu, Q., Ji, A., Qu, C., Chen, H., and Cheng, Z. (2022). Organic single molecule based nano-platform for NIR-II imaging and chemo-photothermal synergistic treatment of tumor. *Biomaterials* 287, 121670. <https://doi.org/10.1016/j.biomaterials.2022.121670>.
  25. Herrmann, I.K., Wood, M.J.A., and Fuhrmann, G. (2021). Extracellular vesicles as a next-generation drug delivery platform. *Nat. Nanotechnol.* 16, 748–759. <https://doi.org/10.1038/s41565-021-00931-2>.
  26. Meng, W., He, C., Hao, Y., Wang, L., Li, L., and Zhu, G. (2020). Prospects and challenges of extracellular vesicle-based drug delivery system: considering cell source. *Drug Deliv.* 27, 585–598. <https://doi.org/10.1080/10717544.2020.1748758>.
  27. Igami, K., Uchiyama, T., Ueda, S., Kamioka, K., Setoyama, D., Gotoh, K., Akimoto, M., Matsumoto, S., and Kang, D. (2020). Characterization and function of medium and large extracellular vesicles from plasma and urine by surface antigens and Annexin V. *PeerJ Anal. Chem.* 2, e4. <https://doi.org/10.7717/peerj-achem.4>.
  28. Zhao, D., Tao, W., Li, S., Chen, Y., Sun, Y., He, Z., Sun, B., and Sun, J. (2021). Apoptotic body-mediated intercellular delivery for enhanced drug penetration and whole tumor destruction. *Sci. Adv.* 7, eabg0880.
  29. Wang, Y., Pang, J., Wang, Q., Yan, L., Wang, L., Xing, Z., Wang, C., Zhang, J., and Dong, L. (2021). Delivering Antisense Oligonucleotides across the Blood-Brain Barrier by Tumor Cell-Derived Small Apoptotic Bodies. *Adv. Sci.* 8, 2004929. <https://doi.org/10.1002/advs.202004929>.
  30. Yu, W., He, X., Yang, Z., Yang, X., Xiao, W., Liu, R., Xie, R., Qin, L., and Gao, H. (2019). Sequentially responsive biomimetic nanoparticles with optimal size in combination with checkpoint blockade for cascade synergistic treatment of breast cancer and lung metastasis. *Biomaterials* 217, 119309. <https://doi.org/10.1016/j.biomaterials.2019.119309>.
  31. Gong, C., Yu, X., You, B., Wu, Y., Wang, R., Han, L., Wang, Y., Gao, S., and Yuan, Y. (2020). Macrophage-cancer hybrid membrane-coated nanoparticles for targeting lung metastasis in breast cancer therapy. *J. Nanobiotechnology* 18, 92. <https://doi.org/10.1186/s12951-020-00649-8>.
  32. Zhou, S., Abdouh, M., Arena, V., Arena, M., and Arena, G.O. (2017). Reprogramming Malignant Cancer Cells toward a Benign Phenotype following Exposure to Human Embryonic Stem Cell Microenvironment. *PLoS One* 12, e0169899. <https://doi.org/10.1371/journal.pone.0169899>.
  33. Wortzel, I., Dror, S., Kenific, C.M., and Lyden, D. (2019). Exosome-Mediated Metastasis: Communication from a Distance. *Dev. Cell* 49, 347–360. <https://doi.org/10.1016/j.devcel.2019.04.011>.
  34. Wu, Q., Zhang, H., Sun, S., Wang, L., and Sun, S. (2021). Extracellular vesicles and immunogenic stress in cancer. *Cell Death Dis.* 12, 894. <https://doi.org/10.1038/s41419-021-04171-z>.
  35. Hanahan, D. (2022). Hallmarks of Cancer: New Dimensions. *Cancer Discov.* 12, 31–46. <https://doi.org/10.1158/2159-8290.CD-21-1059>.
  36. Forster, J.C., Harris-Phillips, W.M., Douglass, M.J., and Bezak, E. (2017). A review of the development of tumor vasculature and its effects on the tumor microenvironment. *Hypoxia* 5, 21–32. <https://doi.org/10.2147/hp.s133231>.
  37. Majidpoor, J., and Mortezaee, K. (2021). Angiogenesis as a hallmark of solid tumors - clinical perspectives. *Cell. Oncol.* 44, 715–737. <https://doi.org/10.1007/s13402-021-00602-3>.
  38. Ma, J., Zhang, Y., Tang, K., Zhang, H., Yin, X., Li, Y., Xu, P., Sun, Y., Ma, R., Ji, T., et al. (2016). Reversing drug resistance of soft tumor-repopulating cells by tumor cell-derived chemotherapeutic microparticles. *Cell Res.* 26, 713–727. <https://doi.org/10.1038/cr.2016.53>.
  39. Wu, M., Liu, X., Bai, H., Lai, L., Chen, Q., Huang, G., Liu, B., and Tang, G. (2019). Surface-Layer Protein-Enhanced Immunotherapy Based on Cell Membrane-Coated Nanoparticles for the Effective Inhibition of Tumor Growth and Metastasis. *ACS Appl. Mater. Interfaces* 11, 9850–9859. <https://doi.org/10.1021/acsami.9b00294>.
  40. Wang, H., Wang, K., He, L., Liu, Y., Dong, H., and Li, Y. (2020). Engineering antigen as photosensitizer nanocarrier to facilitate ROS triggered immune cascade for photodynamic immunotherapy. *Biomaterials* 244, 119964. <https://doi.org/10.1016/j.biomaterials.2020.119964>.
  41. Zheng, L., Hu, X., Wu, H., Mo, L., Xie, S., Li, J., Peng, C., Xu, S., Qiu, L., and Tan, W. (2020). In Vivo Monocyte/Macrophage-Hitchhiked Intratumoral Accumulation of Nanomedicines for Enhanced Tumor Therapy. *J. Am. Chem. Soc.* 142, 382–391. <https://doi.org/10.1021/jacs.9b11046>.
  42. Barenholz-Cohen, T., Merker, Y., Haj, J., Shechter, D., Kirchmeier, D., Shaked, Y., and Weihs, D. (2020). Lung mechanics modifications facilitating metastasis are mediated in part by breast cancer-derived extracellular vesicles. *Int. J. Cancer* 147, 2924–2933. <https://doi.org/10.1002/ijc.33229>.
  43. Mavridi-Printezi, A., Menichetti, A., Mordini, D., and Montali, M. (2023). Functionalization of and through Melanin: Strategies and Bio-Applications. *Int. J. Mol. Sci.* 24, 9689. <https://doi.org/10.3390/ijms24119689>.
  44. Jiang, Q., Liu, Y., Guo, R., Yao, X., Sung, S., Pang, Z., and Yang, W. (2019). Erythrocyte-cancer hybrid membrane-camouflaged melanin nanoparticles for enhancing photothermal therapy efficacy in tumors. *Biomaterials* 192, 292–308. <https://doi.org/10.1016/j.biomaterials.2018.11.021>.
  45. Jiang, Q., Luo, Z., Men, Y., Yang, P., Peng, H., Guo, R., Tian, Y., Pang, Z., and Yang, W. (2017). Red blood cell membrane-camouflaged melanin nanoparticles for enhanced photothermal therapy. *Biomaterials* 143, 29–45. <https://doi.org/10.1016/j.biomaterials.2017.07.027>.
  46. Gujrati, V., Prakash, J., Malekzadeh-Najafabadi, J., Stiel, A., Klemm, U., Mettenleiter, G., Aichler, M., Walch, A., and Ntziachristos, V. (2019). Bioengineered bacterial vesicles as biological nano-heaters for optoacoustic imaging. *Nat. Commun.* 10, 1114. <https://doi.org/10.1038/s41467-019-09034-y>.
  47. Li, Z., Liu, C., Cheng, Y., Li, Y., Deng, J., Bai, L., Qin, L., Mei, H., Zeng, M., Tian, F., Zhang, S., and Sun, J. (2023). Cascaded microfluidic circuits for pulsatile filtration of extracellular vesicles from whole blood for early cancer diagnosis. *Sci. Adv.* 9, eade2819. <https://doi.org/10.1126/sciadv.ade2819>.
  48. Speiser, D.E., Chijioko, O., Schaeuble, K., and Münz, C. (2023). CD4+ T cells in cancer. *Nat. Cancer* 4, 317–329. <https://doi.org/10.1038/s43018-023-00521-2>.
  49. Waldman, A.D., Fritz, J.M., and Lenardo, M.J. (2020). A guide to cancer immunotherapy: from T cell basic science to clinical practice. *Nat. Rev. Immunol.* 20, 651–668. <https://doi.org/10.1038/s41577-020-0306-5>.
  50. Jhunjhunwala, S., Hammer, C., and Delamarre, L. (2021). Antigen presentation in cancer: insights into tumour immunogenicity and immune evasion. *Nat. Rev. Cancer* 21, 298–312. <https://doi.org/10.1038/s41568-021-00339-z>.
  51. Zou, W. (2022). Immune regulation in the tumor microenvironment and its relevance in cancer therapy. *Cell. Mol. Immunol.* 19, 1–2. <https://doi.org/10.1038/s41423-021-00738-0>.
  52. Tie, Y., Tang, F., Wei, Y.-Q., and Wei, X.-W. (2022). Immunosuppressive cells in cancer: mechanisms and potential therapeutic targets. *J. Hematol. Oncol.* 15, 61. <https://doi.org/10.1186/s13045-022-01282-8>.
  53. Buzas, E.I. (2023). The roles of extracellular vesicles in the immune system. *Nat. Rev. Immunol.* 23, 236–250. <https://doi.org/10.1038/s41577-022-00763-8>.
  54. Li, Y., Zhang, K., Wu, Y., Yue, Y., Cheng, K., Feng, Q., Ma, X., Liang, J., Ma, N., Liu, G., et al. (2022). Antigen Capture and Immune Modulation by Bacterial Outer Membrane Vesicles as In Situ Vaccine for Cancer Immunotherapy Post-Photothermal Therapy. *Small* 18, e2107461. <https://doi.org/10.1002/smll.202107461>.
  55. Guo, R., Wang, S., Zhao, L., Zong, Q., Li, T., Ling, G., and Zhang, P. (2022). Engineered nanomaterials for synergistic photo-immunotherapy. *Biomaterials* 282, 121425. <https://doi.org/10.1016/j.biomaterials.2022.121425>.
  56. Shang, T., Yu, X., Han, S., and Yang, B. (2020). Nanomedicine-based tumor photothermal therapy synergized immunotherapy. *Biomater. Sci.* 8, 5241–5259. <https://doi.org/10.1039/d0bm01158d>.

## STAR★METHODS

### KEY RESOURCES TABLE

REAGENT or RESOURCE	SOURCE	IDENTIFIER
<b>Antibodies</b>		
Anti-CD63 antibody	Sangon Biotech	Cat#20-511-241248, RRID:AB_1011736
HRP-conjugated Goat anti-Rabbit IgG	Sangon Biotech	Cat# ZB-2301, RRID:AB_2747412
Anti-ALIX antibody	HUABIO	Cat#A302-938A, RRID:AB_10681518
Anti-Cytochrome C antibody	HUABIO	Cat# ET1610-60, RRID:AB_2940742
Anti-GAPDH Recombinant Rabbit Monoclonal antibody	HUABIO	Cat# HA721131, RRID:AB_3072255
APC anti-mouse CD3	BioLegend	Cat# 100235, RRID:AB_2561455
PerCP Anti-Mouse CD4 Antibody-[GK1.5]	BioLegend	Cat# 100432, RRID:AB_893323
FITC anti-mouse CD45	BioLegend	Cat# 147709, RRID:AB_2563541
PerCP anti-mouse CD11c	BioLegend	Cat# 117326, RRID:AB_2129643
PE anti-mouse F4/80	BioLegend	Cat# 123109, RRID:AB_893498
APC anti-mouse CD86	BioLegend	Cat# 105011, RRID:AB_493343
PE anti-mouse CD8a	BioLegend	Cat# 123109, RRID:AB_893498
<b>Chemicals, peptides, and recombinant proteins</b>		
Albumin-bound paclitaxel	Hunan Kelun Pharmaceutical	H20203443
DAPI	Cell Signaling Technology	Cat#4083S
Dil	Solarbio	Cat#D8700-10mg
Dir	Solarbio	Cat#IC6110
Amiloride HCl dihydrate	Solarbio	Cat#A0080
Chlorpromazine Hydrochloride	Solarbio	Cat#IC0340
Recombinant Murine GM-CSF	PEPROTECH	Cat#315-03
Recombinant Murine IL-4	PEPROTECH	Cat#214-14
<b>Critical commercial assays</b>		
Annexin V-FITC/PI Apoptosis Detection Kit	Yeasen Biotechnology	Cat#40302ES50
Super ECL Prime Supersensitive ECL chemiluminescence	SEVEN BIOTECH	Cat#SW133-01
<b>Experimental models: Cell lines</b>		
Mouse:4T1	Shanxi Provincial Key Laboratory of Nanoimaging and Drug Delivery	N/A
<b>Experimental models: Organisms/strains</b>		
BALB/C nude mice (male)	Vital River	N/A
C57BL/6 mice(male)	Vital River	N/A
<b>Software and algorithms</b>		
SPSS 18.0	IBM	N/A
GraphPad Prism 8.3.0	GraphPad	N/A
Adobe Photoshop CS6	ADOBE SYSTEMS INCORPORATED	N/A

## RESOURCE AVAILABILITY

### Lead contact

Further information and requests for resources and reagents should be directed to and will be fulfilled by the lead contact, Ruiping Zhang ([zrp\\_7142@sxmu.edu.cn](mailto:zrp_7142@sxmu.edu.cn)).

### Materials availability

The EPM are available on a reasonable request from the [lead contact](#), Ruiping Zhang ([zrp\\_7142@sxmu.edu.cn](mailto:zrp_7142@sxmu.edu.cn)).

### Data and code availability

- All data reported in this paper will be shared by the [lead contact](#), Ruiping Zhang ([zrp\\_7142@sxmu.edu.cn](mailto:zrp_7142@sxmu.edu.cn)).
- This paper does not report original code.
- Any additional information required to reanalyze the data reported in this paper is available from the [lead contact](#) upon request.

## EXPERIMENTAL MODEL AND STUDY PARTICIPANT DETAILS

### Animals and ethics statement

6 week old male BALB/c mice (18–22 g) and 4 week old male C57BL/6 mice (15–17 g) were acquired from Vital River (Beijing, China) and fed in SPF-grade animal rooms throughout the experiment. The animal study performed was authorized by The Ethics Committee of Shanxi Medical University.

## METHOD DETAILS

### Cell culture

Mouse breast cancer cell line, 4T1, was purchased from the Cell Bank of the Chinese Academy of Sciences and stored at the Shanxi Provincial Key Laboratory of Nanoimaging and Drug Delivery. The 4T1 cells were grown in RPMI 1640 supplemented with 1% penicillin/streptomycin and 10% fetal bovine serum (Gibco, Australia).

### Preparation of EPM

In this study, 4T1 cells plated in 150 cm<sup>2</sup> were grown in FBS-free RPMI 1640 medium for 20 h after exposure to ultraviolet irradiation for 1 h to induce the apoptosis of secretory vesicles. To remove cells and cell debris, the cell culture medium was obtained, centrifuged at 2300 rpm for 8 min, and then centrifuged at 17000 g for 2 min. The supernatant was centrifuged at 17000 g for 90 min and washed thrice with PBS to obtain the purified vesicles. The BCA method was used for a quantitative analysis after resuspension in deionized water. To generate the EPM, 1 mg of vesicles, 20 mg of PA and 1 mg of melanin were compressed repeatedly over a 200 nm porous polycarbonate membrane and centrifuged at 17000 g for 90 min. The unloaded PA and melanin were removed. The hollow vesicle samples can be stored for a long duration at –80°C.

### Transmission electron microscope (TEM) and dynamic light scattering (DLS)

The samples were deposited onto a carbon-coated copper grid, stained for 1 min with 10 μL 0.1% uranyl acetate, and rinsed thrice with PBS. The field of view was captured using a TEM. DLS was performed to determine the hydrodynamic diameter and zeta potential of EVs and the EPM.

### High-Performance Liquid chromatography (HPLC)

To identify the concentration of Paclitaxel in the EPM, LC-MS (column: Alphasil VC-C18) was performed, 10 mL of Paclitaxel solution with a known concentration was prepared and diluted into various concentration gradients. The absorbance of various concentrations of Paclitaxel at 230 nm was measured using HPLC, and a Paclitaxel standard curve was constructed. Subsequently, the EPM was dissolved in acetonitrile and ultrasonically dissolved, and the supernatant was obtained for LC-MS/MS analysis. Acetonitrile and deionized water were used as the mobile phases. The flow rate was 1.0 mL/min, the injection volume was 10 μL, and the column temperature was 30°C. To calculate the total amount of Paclitaxel in the EPM (M1), the total amount of Paclitaxel in the EPM (M1) and the total amount of Paclitaxel added initially (M2) were used. Subsequently, the encapsulation efficiency (EE) was calculated as follows: encapsulation efficiency =  $M1/M2 \times 100\%$ .

### Cell apoptosis

In this study,  $2 \times 10^5$  4T1 cells were sown in six-well plates and cultivated for 24 h at 37°C and 5% CO<sub>2</sub>. The treatment groups were as follows: PBS, PBS+Laser, PA, EVs loaded with melanin (EM), EM + Laser, EPM, and EPM+Laser. In each group, the effective medication concentration of PA was 0.7 mg/mL, whereas the concentration of melanin was 100 μg/mL. Set three replicates for each group. After 24 h of drug incubation, the cells were digested with trypsin without EDTA, washed with PBS once, resuspended in 100 μL of 1×binding buffer, added with 5 μL of Annexin V/FITC and 5 μL of propidium iodide solution, incubated at room temperature in the dark for 5 min, added with 400 μL of PBS, and immediately detected via flow cytometry.

### Flow cytometry and confocal microscopy

A total of  $2 \times 10^5$  cells were seeded in 12-well plates and cultured for 24 h at 37°C and 5% CO<sub>2</sub>. Dir (100 μM)/Dil (100 μM)-labeled EPM solution was added and incubated for 0.5 h, 1.5 h, and 3 h, separately. The cells were obtained and washed with PBS for quantitative fluorescence analysis, and the percentage of positive cells was determined via flow cytometry. To clarify the internalization mechanism of the EPM in

4T1 cells, two endocytosis inhibitors, that is, amiloride (25  $\mu\text{M}$ ) and chlorpromazine (100  $\mu\text{M}$ ), were pre-incubated with Dir-labeled/GFP-labeled EPM for 1 h at 37°C. Simultaneously, 4T1 cells were treated for 1 h with Dir-labeled EPM at 37°C and 4°C, separately. After washing with PBS, the cells were obtained and analyzed via flow cytometry. Puromycin screening and large-scale amplification culture were used to create GFP-labeled EVs after 4T1 cells were infected with LV3 lentivirus (GenePharma, Shanghai) producing GFP protein.

Flow cytometry was used to examine DCs labeled with Percp anti-mouse CD11c, APC anti-mouse CD86, and PE anti-mouse F4/80. Mouse tumor tissue cells were labeled with APC anti-mouse CD3, PerCP anti-mouse CD4 [GK1.5], FITC anti-mouse CD45, or PE anti-mouse CD8a. Cytological analysis was performed via flow cytometry.

For confocal detection, the cells were washed several times with PBS, fixed with 4% paraformaldehyde solution, stained with 300  $\mu\text{L}$  of 400 nM DAPI, and imaged with Confocal laser scanning microscope (CLSM) (FV1200, Olympus, Japan) using 514 nm and 405 nm laser.

### Western blot

The cell precipitate was treated with an appropriate amount of RIPA buffer containing protease and phosphatase inhibitors, and the total protein was extracted via incubation on ice. The protein concentration was detected using a BCA assay. The protein was transferred to a PVDF membrane after separation on a 10% SDS-polyacrylamide gel. After 2 h of blocking with 5% skim milk at room temperature, the protein was incubated with specific antibodies overnight at 4°C. The anti-CD63, anti-ALIX, anti-cytochrome C and anti-Annexin V antibody used had primary antibody ratios of 1:800, 1:500, 1:1000, and 1:500 respectively. TBST was washed and incubated with HRP secondary antibody (Abcam, Cambridge, UK, 1:2000) at room temperature for 2h. TBST was washed and the images were collected and analyzed using ECL development instrument (Tanono-4600SF).

### Photothermal activity of EPM

EPM aqueous solutions of different concentrations (200, 100, 50, 25, 12.5, and 0  $\mu\text{g}/\text{mL}$ ) were poured into a 200  $\mu\text{L}$  EP tube and irradiated with an 808nm laser at 1  $\text{W}/\text{cm}^2$  for 5 min. Simultaneously, a 100  $\mu\text{g}/\text{mL}$  EPM aqueous solution was irradiated for 5 min at different laser power densities (0.25, 0.5, 0.75, and 1.0  $\text{W}/\text{cm}^2$ ). An infrared thermal imaging camera (Ti400) was used to monitor thermal images and temperature changes every 10 s. The EPM solution (100  $\mu\text{g}/\text{mL}$ ) was irradiated with a laser (808 nm, 1  $\text{W}/\text{cm}^2$ ) to acquire the heating and cooling curves. When the solution reached a steady maximum temperature, the laser was shut off and the solution was cooled to room temperature. DI water was used as the control.

### Animal model

After 7 days of adaptive feeding, the fifth pair of mammary glands on the right leg of each mouse was depilated with depilatory cream one day before cancer cell inoculation. The mice were anesthetized and disinfected with 5% chloral hydrate. A small incision was created above the fifth set of mammary glands on the right leg of the mouse. A suture needle was used to inoculate 50  $\mu\text{L}$  ( $1 \times 10^5$  cells) of 4T1 cell suspension into the mouse mammary pad. When the tumor volume reached approximately 100  $\text{mm}^3$ , we focused on tumor development in subsequent experiments.

### In-vivo photoacoustic imaging

Mice with 4T1 orthotopic breast cancer ( $\sim 100 \text{mm}^3$ ) were injected with 50 $\mu\text{L}$  of PBS or EPM to identify tumor enrichment (EPM treatment group  $n = 4$ , PBS treatment group  $n = 3$ ). An MSOT scanner was used to capture images of the tumor region before and after injection at 2 h, 4 h, 8 h, 12 h, and 24 h within an NIR excitation wavelength range of 680–980 nm. In addition, the photoacoustic signal strengths at different points around the tumor site were quantified.

### Anti-tumor effect in vivo

The tumor volume and body weight were measured at regular intervals. When the tumor volume reached approximately 100  $\text{mm}^3$ , the mice were classified into eight groups ( $n = 5$  per group). Each group received either PBS/PA/EM/EPM peritumoral injection or laser treatment. Three hours after injection, the tumor was irradiated for 5 min with a continuous wave laser (1.0  $\text{W}/\text{cm}^2$ , 808 nm). An infrared thermal imager was used to record the thermal images and temperature changes during irradiation. Following therapy, the tumors were obtained and histopathologically examined based on Hematoxylin and eosin(H&E) staining.

### In-vivo safety

Six-week-old male BALB/c mice ( $n = 3$ ) were injected with 200  $\mu\text{L}$  of the EPM and PBS, respectively. The mice were sacrificed after 24 h, blood samples from each group of mice were taken and centrifuged to obtain serum, and the AST, ALT, Scr, and BUN levels were measured. The major organs of the mice were stained with H&E. The effects on the mouse liver, renal function, and other organs were comprehensively evaluated. Under an NIR excitation wavelength of 808 nm, an MSOT scanner was used to take pictures of the organs and tissues of mice ( $n = 3$ ) with 4T1 orthotopic breast cancer (100  $\text{mm}^3$ ) before and after intravenous injection at 1 h, 2 h, 4 h, 8 h, 10 h, 12 h, 24 h, and 48 h. After 48 h, the mice were sacrificed, and the enrichment of EPM in separated tissues and organs under 808 nm NIR irradiation was obtained.

### Isolation of mouse immune cells

We isolated DCs from the bone marrow of C57BL/6 male mice (4 week old). Euthanize C57BL/6J mice (4 weeks old), remove all femurs and tibias, disinfect the bones, and put them in a culture dish with PBS. Repeat the procedure of flushing the bone marrow into the dish with a syringe until the bones are entirely white. Collect the bone marrow suspension and strain it through a 200-mesh cell strainer to eliminate tiny shards and muscle tissue. Centrifuge the filtrate at 1200 rpm for 5 min before adding red blood cell lysis buffer. Incubate for 3–5 min at room temperature before diluting with PBS to stop the lysis effect. Centrifuge the cells for 5 min at 1200 rpm, then wash once with PBS before culturing in an RPMI-1640 medium containing 10% fetal bovine serum, 1% penicillin/streptomycin, GM-CSF (20 ng/mL), and IL-4 (10 ng/mL).

T cell infiltration was detected in the mouse tumor tissues. Physical grinding and filtration were performed to isolate the tumor cells after the tumor tissues of the mice were removed. The cells were centrifuged at 400 g for 5 min for precipitation, and washing with PBS.

### Preparation of conditioned medium

To detect the maturation effect of the EPM on DCs. 4T1 cells were seeded at a density of  $5 \times 10^5$  in six-well plates. After 5 h of incubation with the EPM, the supernatant was discarded and replaced with fresh basic culture medium for 24 h. The cell culture medium was obtained at 4°C and centrifuged at 2000 rpm for 10 min, and the precipitate was discarded and centrifugation was performed at 12000 rpm for 20 min. Subsequently, the supernatant was obtained, filtered using a 0.22  $\mu\text{m}$  filter membrane, and stored at 4°C.

### QUANTIFICATION AND STATISTICAL ANALYSIS

All data are presented as mean  $\pm$  standard deviation. The Student's *t* test and ANOVA were used to compare the mean values. Statistical analyses were performed using SPSS version 18.0. Statistical significance was set at  $p < 0.05$ . \* $p < 0.05$ , \* \* $p < 0.01$ , and \* \* \* $p < 0.001$ .